Non-oxidative dehydrogenation of ethane to ethylene over ZSM-5 zeolite supported iron catalysts

Lu-Cun Wang[a,1], Yunya Zhang[a,b,1], Jiayi Xu[c], Weijian Diao[b], Stavros Karakalos[b], Bin Liu[c], Xueyan Song[d], Wei Wu[a], Ting He[a], Dong Ding[a,*]

[a] Energy & Environmental Science and Technology, Idaho National Laboratory, Idaho Falls, ID, 83401, USA
[b] Department of Chemical Engineering, University of South Carolina, Columbia, SC, 29208, USA
[c] Department of Chemical Engineering, Kansas State University, Manhattan, KS, 66506, USA
[d] Department of Mechanical and Aerospace Engineering, West Virginia University, Morgantown, WV, 26506, USA

ABSTRACT

The shale gas boom has stimulated tremendous interests in ethylene production using ethane as the feedstock. Catalytic non-oxidative ethane dehydrogenation (EDH) to ethylene represents a viable strategy to improve the process energy efficiency and to minimize the environmental impact. The breakthroughs in catalyst design play a key role in the successful development of this process. Herein, we demonstrate that iron supported on ZSM-5 zeolite (Fe/ZSM-5) is a highly efficient catalyst for the EDH reaction. Under comparable conditions, Fe/ZSM-5 exhibits superior activity and stability over various metal (Pt) or metal oxide catalysts (Zn, Ga, Cr, Mo) supported on ZSM-5. The use of ZSM-5 instead of conventional γ-Al_2O_3 as the support for Fe catalysts is critical to achieve high activity and selectivity in the EDH reaction. Detailed structure characterizations combined with density functional calculations indicate that iron oxides in the as-prepared Fe/ZSM-5 catalysts are reduced to iron metal and then carburized under reaction condition, which accounts for the excellent activity and stability for the EDH reaction. Compared with Fe/Al_2O_3, the relatively weaker binding strength of ethylene and the weaker surface acidity on Fe/ZSM-5 allow facile desorption of ethylene, which suppresses its consecutive transformation into higher hydrocarbons and carbon deposits, resulting in higher ethylene selectivity.

1. Introduction

Ethylene is one of the most important building blocks for chemical production. The industrial-scale production of ethylene is conventionally practiced by steam cracking of ethane derived from crude oil. This process is highly energy intensive, requiring high temperature (> 800 °C) with low energy efficiency due to undesired side reactions and severe coke formation. Particularly, this process contributes significantly to CO_2 and NO_x emissions [1–3]. Therefore, more energy efficient and environmentally benign processes for ethylene production are desirable. In recent years, there has been an oversupply of ethane resulting from the shale gas revolution in the United States, which significantly lowered its cost and stimulated great interest in exploiting its potential as a direct feedstock for ethylene production. In this context, catalytic dehydrogenation of ethane to ethylene via oxidative or non-oxidative routes holds great promise in the reduction of process energy consumption and environmental impact [1–3].

Oxidative dehydrogenation (ODH) of ethane has been the subject of intensive research efforts [1,3,4], due to its relatively higher single-pass conversions of ethane as well as less external energy input needed. However, the highly exothermic nature of the ODH process also brings about great challenges in heat recovery and process safety control. The tradeoff between ethane conversion and ethylene selectivity owing to the over-oxidation is another factor that hinders its commercial implementation. In contrast, non-oxidative ethane dehydrogenation (EDH) can avoid most of the issues associated with ODH. From a practical point of view, EDH process could be more attractive for the upgrading of ethane in stranded gases including flaring gas in shale oil field, refinery off-gas, shale gas in geographically disadvantaged locations, etc. [5]. The drawbacks of EDH are relatively high energy demand, low single-pass conversion limited by the thermodynamic equilibrium, and rapid coking-induced deactivation of the catalysts [2,3]. Potential solutions could be separation of H_2 product from the product mixture by applying membrane reactors to shift the reaction

equilibrium toward ethylene formation [2,6–8] and developing highly selective and coke-resistant catalysts [3,9–12].

Pt- and CrO_x-based catalysts, typically supported on Al_2O_3 or aluminates such as $MgAl_2O_4$ [1,2], are the most extensively studied systems for non-oxidative dehydrogenation of light alkanes, propane in particular [1–3,13]. Other metal oxides, such as V, Ga, Zn, and Mo oxides, have also been reported to be of great potential [3,14–21]. For the EDH reaction, Pt-based catalysts with promoters such as Zn [22], Sn [9,23], Ga [10,11], and In [12] have been investigated and they showed either high activity or high selectivity of ethylene. Nevertheless, these catalysts usually lose over 60% of the initial activity during the first few hours of reaction due to coke formation accompanied by sintering of Pt particles [1,2,9,10]. Therefore, the development of alternative catalysts with both active and durable performance for EDH reaction are still imperative.

Due to their earth abundance and low toxicity, Fe-based catalysts have been widely used in various conversion processes including dehydrogenation and hydrocarbon synthesis. For instance, Al_2O_3-supported Fe oxides have long been known as excellent catalysts in ethylbenzene and ethyltoluene dehydrogenation [24,25], but they are usually regarded as poor catalysts for dehydrogenation of light alkanes [1,26]. It is important to note that the catalytic performances of Fe catalysts could be significantly affected by the type and properties of supporting material [27–30]. Recently, Fe-substituted ZSM-5 has been investigated for non-oxidative propane dehydrogenation, achieving a high propylene selectivity (78–85%) with modest conversion (ca. 3.6%) [31], suggesting that Fe supported on zeolite materials may be promising catalytic systems for selective alkane dehydrogenation.

In this work, we have successfully demonstrated that the Fe oxides can be used as highly active, selective, and stable catalysts for EDH reaction when supported on ZSM-5 zeolite (Fe/ZSM-5). The catalytic performances of Fe/ZSM-5 under steady state surpass that of conventional Pt or metal oxides including Zn, Cr, Mo, Ga, etc., which have been well documented to be good catalysts for dehydrogenation of light alkanes. The influence of iron loading, support material, and reaction parameters on the catalytic properties of Fe/ZSM-5 catalysts in EDH was investigated in detail. The textural, structural, and the surface properties of the as-prepared and used Fe/ZSM-5 catalysts were characterized using various techniques including X-ray diffraction (XRD), transmission electron microscopy (TEM), ammonia/ethylene temperature programmed desorption (C_2H_4/NH_3-TPD), and in situ X-ray photoelectron spectroscopy (XPS), etc. The nature of active sites and the origin of the remarkable support effect are discussed based on the experimental results as well as density functional theory (DFT) calculations.

2. Experimental

2.1. Preparation of catalysts

Two sets of ZSM-5 (CBV 5524 G, Si/Al = 25, surface area 425 $m^2 g^{-1}$, Zeolyst International) supported catalysts were prepared by incipient wetness impregnation method. In the first catalyst set, the Fe/ZSM-5 catalysts with different Fe loadings (0.5, 2.0 and 10 wt%) using aqueous solutions of iron nitrate $Fe(NO_3)_2 \cdot 9H_2O$ (Alpha Aesar, 99.9%). In the second catalyst set, different metal catalysts supported on ZSM-5 were obtained using aqueous solutions of zinc nitrate $Zn(NO_3)_2 \cdot 6H_2O$ (Alpha Aesar, 99.9%), gallium nitrate $Ga(NO_3)_3 \cdot 8H_2O$ (Alpha Aesar, 99.999%), Mo heptamolybdate $(NH_4)_6Mo_7O_{24} \cdot 4H_2O$ (Acros Organics, 99.9%), chromium nitrate $Cr(NO_3)_3 \cdot 9H_2O$ (Acros Organics, 99.9%), tetraammineplatinum nitrate $Pt(NH_3)_4(NO_3)_2$ (Alpha Aesar, 99.9%) with the nominal metal loading being kept constant at 2.0 wt%. After impregnation, the catalysts were dried at room temperature in air overnight and further ramped to 120 °C at 1 °C/min in flowing air and held for 5 h. After drying, the samples were calcined in flowing air by ramping to 600 °C at 1 °C/min and holding for 2 h.

The Al_2O_3 supported Fe catalyst (2Fe/Al_2O_3), with Fe loading of 2.0 wt%., was prepared by incipient wetness impregnation using aqueous solution of iron nitrate and γ-Al_2O_3 (AEROXIDE Alu 130, surface area 130 $m^2 g^{-1}$). After impregnation, the catalysts were dried at 100 °C overnight followed by calcination in flowing air by ramping to 600 °C at 10 °C/min and holding for 6 h.

2.2. Characterization

Textural properties of the supports and catalysts were measured with a Micromeritics ASAP 2020 analyzer by nitrogen adsorption at −196 °C. The samples were outgassed at 150 °C for 270 min before measurements. This instrument employed the Brunauer − Emmett − Teller (BET) method by measuring the quantity of nitrogen absorbed at −196 °C. The cumulative pore volumes and pore sizes were obtained by the Barrett − Joyner − Halenda (BJH) method from the desorption branches of the adsorption isotherms. The chemical composition of the samples was determined by an ICAP 6500 inductively coupled plasma optical emission spectrometer (ICP-OES).

Powder XRD measurements were performed with 2θ values between 10 and 60° by using a Rigaku Miniflex II diffractometer employing the graphite filtered Cu Kα radiation (λ = 1.5406 Å). The average crystallite sizes of Fe oxides were calculated from the diffraction peak at 35.71° by using the Scherrer equation: $D = K\lambda/(\beta \cos\theta)$, in which $K = 0.89$ is the Scherrer's constant, and β is the FWHM.

TEM was conducted to characterize the morphology of catalysts. Chemical analysis was carried out under TEM using energy dispersive X-ray Spectroscopy (EDS). The as-prepared samples were spread onto the Mo-grid for TEM imaging with a JEM-2100 transmission electron microscope at 200 kV. The used samples were dispersed in methanol and supported on carbon-film-coated copper grids before TEM images were recorded with a FEI Tecnai G2 F30 FEG STEM at an accelerating voltage of 300 kV.

TGA (STA449F3 NETZSCH Corp.) was used to investigate the carbon deposition of spent catalysts. The sample was preheated at 80 °C for 30 min in Ar (50 mL/min). Then the sample was heated to 780 °C at a rate of 10 °C/min in air (50 mL/min).

The temperature programmed desorption (TPD) experiments were conducted with a high precision quadrupole mass spectrometer (QMS; Inficon Transpector 2) to continuously monitor all volatile species during the TPD experiment. For the NH_3-TPD experiments, 100 mg of each sample was pretreated at 200 °C for 1 h under He and cooled down to 150 °C, then exposed to 1%NH_3/He flow for 45 min until saturation, followed by purging with He for at 150 °C for 90 min. The temperature was then ramped to 700 °C at 10 °C/min and held for 2 h until complete desorption of NH_3. For the C_2H_4-TPD experiments, 100 mg of each sample was pretreated at 600 °C for 1 h under 10%H_2/He and cooled down to 50 °C in He, then exposed to C_2H_4 flow for 30 min until saturation, followed by purging with He for 2 h at 50 °C. The temperature was then ramped to 700 °C at 10 °C/min and held for 2 h until complete desorption of C_2H_4.

XPS measurements were performed using a Kratos AXIS Ultra DLD XPS system with a monochromatic Al Kα source operated at 15 keV and 150 W and a hemispherical energy analyzer. The X-rays were incident at an angle of 45° with respect to the surface normal. Analysis was performed at a pressure below 1×10^{-9} mbar. High-resolution core level spectra were measured with the pass energy of 40 eV and analysis of the data was carried out using XPSPEAK41 software. Nonlinear Shirley functions were used for background subtraction during the XPS peak fitting. For identical species, both the peak position and full width at half maximum (FWHM) were constrained to ± 0.2 eV during the fitting for all samples. A fixed Lorentzian/Gaussian ratio of 40/60 and 20/80 was used for the fitting of Fe2p and C1s peaks, respectively. The typical deconvolution parameters for fitting of Fe2p signals are also be provided in Table S1 in the Supplementary Material. The XPS experiments were performed while using an electron gun directed on the

sample, for charge neutralization. The in-situ gas treatments of the catalysts were conducted in a catalysis cell attached to the XPS analysis chamber. All binding energies (BE) were referenced to the zeolitic Si 2p lines at 103.4 eV for Fe/ZSM-5 samples and to the Al 2p lines at 74.5 eV for 2Fe/Al$_2$O$_3$.

2.3. Computational method

Density functional theory (DFT) calculations were performed using Vienna ab initio simulation package (VASP) [32]. The generalized gradient approximation Perdew-Burke-Ernzerhof (GGA-PBE) functional was used to account for the electron exchange-correlation effects [33]. The iron-electron interactions were treated with the projector augmented wave (PAW) method [34]. All the calculations are spin polarized. The energy cutoff for the plane wave function was 400 eV. The break condition for self-consistent iterations is 1×10^{-5}. Ionic relaxation was stopped when the forces on all atoms were smaller than -0.02 eV/Å. The gamma k-point was employed throughout entire DFT calculations. More details are provided in the Supplementary Material.

2.4. Catalyst testing

Catalytic tests were carried out at the atmospheric pressure in a quartz tubular fixed-bed reactor with 7 mm inner diameter and 46 cm length. A mixture of 100 mg catalysts and 200 mg quartz sand with 50–70 mesh size distribution was loaded in the reactor. The temperature of the catalyst bed was measured by a thermocouple centered axially inside the reactor. The product gas was analyzed by an online GC equipped with two flame ionization detectors (RTX-1 Pona column and Alumina Bond column). The carbon balance calculated from the ratio of sum of the reaction products to educts was over 95% for all catalysts tested during reaction process. The overall ethane conversion (X_{C2H6}) was calculated considering conversion to all products including coke according to Eq. (1):

$$X_{C2H6} \ (\%) = ([C_2H_6]_{in} - [C_2H_6]_{out})/ \ [C_2H_6]_{in} \cdot 100\% \quad (1)$$

where $[C_2H_6]_{in}$, $[C_2H_6]_{out}$ are ethane concentration in the inlet and outlet gas flow. The selectivity to ethylene (S_{C2H4}) and methane (S_{CH4}) was determined from Eqs. (2) and (3):

$$S_{C2H4} \ (\%) = [C_2H_4]/([C_2H_6] \times X_{C2H6}) \cdot 100\% \quad (2)$$

$$S_{CH4} \ (\%) = (0.5 \times [CH_4])/([C_2H_6] \times X_{C2H6}) \cdot 100\% \quad (3)$$

where $[C_2H_4]$, $[CH_4]$ are ethylene and methane concentration in the outlet gas flow, respectively.

3. Results and discussion

3.1. Catalytic performances of Fe/ZSM-5 in EDH reaction

The activity and selectivity of Fe/ZSM-5 catalysts with varied Fe

loadings as a function of time on stream are depicted in Fig. 1. For all the three catalysts, the activity increased rapidly with time initially and reached a maximum in about 30 min, followed by a smooth decay to different extents. The ethane conversion was 6%, 17%, and 28% at time 30 min and then slightly decreased to 5%, 15%, and 22% after reaction for 270 min for 0.5, 2, and 10Fe/ZSM-5, respectively (Fig. 1A). Interestingly, the corresponding specific reaction rate of ethane normalized by Fe content was almost the same for 0.5 and 2Fe/ZSM-5 (˜0.33 mmol$_{C2H6}$·s^{-1}·g$_{Fe}$$^{-1}$) but significantly higher by a factor of 3 than that of 10Fe/ZSM-5 (˜0.1 mmol$_{C2H6}$·s^{-1}·g$_{Fe}$$^{-1}$, see Table 1). The ethylene selectivity over all the three catalysts was about 70% after reaction for 270 min. Note that negligible activity was obtained on the parent ZSM-5 zeolite without Fe (Fig. 1A).

In addition to the notable influence of Fe loading, we also found that the catalytic performance of Fe catalyst for EDH reaction was strongly affected by the type of support material. With the same Fe loading (2 wt.%), the activity of Fe catalyst supported on ZSM-5 zeolite was by a factor of 5 higher than that supported on commercial γ-Al$_2$O$_3$, which had an ethane conversion of only about 3% after reaction for 270 min. In addition, the selectivity to ethylene on Fe/ZSM-5 was also remarkably superior to that on Fe/Al$_2$O$_3$, being only ˜17% for the latter (Fig. 1B and Table 1).

The ethane conversion and selectivity to ethylene over Fe/ZSM-5 were also compared with various metal and metal oxide catalysts supported on ZSM-5 (see Table 2). Among all the catalysts tested, Pt/ZSM-5 exhibited the highest activity at time zero, with ethane conversion of ca. 45%. However, Pt/ZSM-5 underwent rapid deactivation in the first 2 h of reaction, losing almost 90% of its initial activity. An in-house-prepared PtSn/Al$_2$O$_3$ catalyst was also tested in EDH reaction. Analogous to Pt/ZSM-5, deactivation by ca. 60% was observed on PtSn/Al$_2$O$_3$ despite its high initial ethane conversion of ca. 35% (Fig. S1). Similar results have been reported previously for Pt or PtSn catalysts supported on Mg(Al)O hydrotalcite in EDH reaction under comparable conditions, which deactivated by 70–80% in the first 30 min on stream [9]. Concomitantly, the selectivity to ethylene also rapidly decreased to 40% in 270 min. Zn/ZSM-5 is the second most active catalyst initially in the series, giving an initial ethane conversion of ca. 35% and selectivity to ethylene of 45%. Nevertheless, pronounced deactivation by 53% also occurred for this catalyst, reaching an ethane conversion of 16.6% after 270 min on stream. As for the other three ZSM-5 supported metal oxide catalysts, namely, Ga/ZSM-5, Cr/ZSM-5 and Mo/ZSM-5, much lower activities were obtained, with a maximum ethane conversion of ca. 10% or less. The selectivity to ethylene was also significantly lower, below 45%. In addition, rapid deactivation was observed for Mo/ZSM-5, by about 57% in 270 min of reaction.

Kinetic studies have been performed on 2Fe/ZSM-5 to further investigate the effect of several parameters, including the reaction temperature, H$_2$/C$_2$H$_6$ ratio, flow rate and the concentration of ethane, on the production rate and selectivity of the ethylene product. Arrhenius plots have yielded a comparable apparent activation energy (E_a) of ˜110 kJ·mol^{-1} within the experimental error for the Fe/ZSM-5 catalysts

Fig. 1. (A) C$_2$H$_6$ conversion and (B) C$_2$H$_4$ selectivity of Fe/ZSM-5 and Fe/Al$_2$O$_3$. (black) 0.5Fe/ZSM-5, (red) 2Fe/ZSM-5, (blue) 10Fe/ZSM-5, (green) 2Fe/Al$_2$O$_3$, (purple) pure ZSM-5. Reaction conditions: 0.1 g catalyst, 9 vol.% C$_2$H$_6$/Ar, 60 mL/min, 600 °C (For interpretation of the references to colour in this figure legend, the reader is referred to the web version of this article).

Table 1
Catalytic properties of various Fe-based catalysts.

Catalyst	X_{C2H6} [a] (%)	Rate [a] (mmol$_{C2H6}$·s^{-1}·g$_{Fe}$$^{-1}$)	Sel_{C2H4} [a] (%)	E_a [b] (kJ·mol^{-1})	Deacti-vation [a], [c] (%)	Coke deposition [d] (g·g$_{cat}$$^{-1}$)
0.5Fe/ZSM-5	5.0	0.336	71.9	100 ± 12	15	0.005
2Fe/ZSM-5	15.0	0.324	68.8	110 ± 10	12	0.049
10Fe/ZSM-5	21.8	0.099	71.6	110 ± 25	23	0.172
2Fe/Al$_2$O$_3$	3.2	0.061	17.0	141 ± 22	5	0.268

[a] Reaction conditions: after reaction for 270 min, 0.1 g catalyst, 9 vol.% C$_2$H$_6$/Ar, 60 mL/min, 600 °C.
[b] Apparent activation energy determined from the reaction rate of C$_2$H$_6$ at different temperatures.
[c] Relative to the initial ethane conversion at time 30 min on stream.
[d] Determined from TGA analysis after reaction for 15 h.

Table 2
Catalytic performances of various ZSM-5 supported catalysts. [a]

Catalyst	$X_{C2H6,initial}$ [b] (%)	$X_{C2H6,270min}$ [c] (%)	Sel_{C2H4} [d] (%)	Deactivation [e] (%)
Fe/ZSM-5	9.9	15.0	68.8	12
Pt/ZSM-5	44.6	4.2	40.1	91
Zn/ZSM-5	35.4	16.6	68.0	53
Ga/ZSM-5	7.5	6.9	44.9	8
Cr/ZSM-5	3.2	4.4	39.6	12
Mo/ZSM-5	11.4	4.9	36.2	57

[a] Reaction conditions: 0.1 g catalyst, 9 vol.% C$_2$H$_6$/Ar, 60 mL/min, 600 °C.
[b] C$_2$H$_6$ conversion at time zero.
[c] C$_2$H$_6$ conversion at time 270 min.
[d] C$_2$H$_4$ selectivity at time 270 min.
[e] Based on the maximum activity in the first 30 min of reaction.

Table 3
Physicochemical properties of as-prepared Fe catalysts.

Catalyst	Fe loading [a] (wt%)	S_{BET} [b] (m^2·g^{-1})	V_{total} [b] (cm^3·g^{-1})	$V_{micropore}$ [c] (cm^3·g^{-1})	Total acidity [d] (mmol$_{NH3}$·g^{-1})
ZSM-5	–	425	0.23	0.14	1.83
0.5Fe/ZSM-5	0.61	393	0.16	0.10	1.69
2Fe/ZSM-5	1.9	352	0.14	0.09	1.35
10Fe/ZSM-5	9.0	345	0.18	0.08	0.76
2Fe/Al$_2$O$_3$	2.1	128	0.67	0.02	3.85

[a] Determined by ICP-OES analysis.
[b] Total pore volume.
[c] Volume of micropores.
[d] Determined from NH$_3$-TPD.

regardless of the Fe loading (Table 1). Compared with Fe/ZSM-5, a relatively higher E_a, ~140 kJ mol^{-1}, was obtained for 2Fe/Al$_2$O$_3$. The production rate of ethylene can be effectively enhanced by reducing the H$_2$ content in the feed gas, lowering the space velocity, and increasing the ethane concentration (see Fig. S2 in the Supplementary Material). Similar effects of H$_2$ addition and the flow rate of ethane on the activity and selectivity in EDH reaction has also been reported on the PtSn/Mg (Al)O catalyst [9]. Note that the ethane concentration has important effects on the product distribution. While ethylene was still the major product, higher hydrocarbons were also detected and became more abundant with increasing ethane concentration, including propylene, butylene, and even aromatics such as benzene and toluene. The absolute selectivity to these byproducts could amount to ca. 50% when pure ethane was used as the feed. This result is not surprising considering the existence of zeolitic acid sites on the ZSM-5 support (see the NH$_3$-TPD results below) which could catalyze consecutive transformations of the ethylene product via hydrogenolysis, cracking, oligmerization, isomerization, alkylation, etc. [35,36].

3.2. Textural properties and surface acidity of Fe catalysts

The textural properties of Fe/ZSM-5, 2Fe/Al$_2$O$_3$, and the parent ZSM-5 are summarized in Table 3. The actual Fe content for each Fe/ZSM-5 catalyst is close to the nominal value. The N$_2$ physisorption on Fe/ZSM-5 catalysts shows an adsorption branch of type I and a H4 type hysteresis, typical for microporous materials (Fig. 2) [37]. The quantity of adsorbed nitrogen slightly decreases as the Fe content increases, probably due to a partial blockage of the pore structures by Fe particles. It is also likely that part of the Fe species migrated into the zeolitic channels, lowering the N$_2$ adsorption capacity in the micropores. This is supported by the fact that the introduction of Fe caused a moderate decrease in both the BET surface area and the micropore volumes (Table 3). In contrast, 2Fe/Al$_2$O$_3$ exhibited a hysteresis loop in the range of $0.8 \leq p/p_0 \leq 0.97$, a type IV isotherm, characteristic of mesoporous structure [37]. The surface area of 2Fe/Al$_2$O$_3$ is ca. a third of that for Fe/ZSM-5 catalysts.
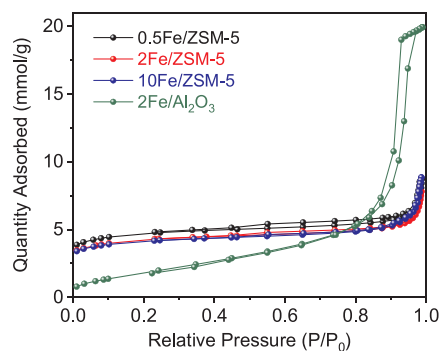

Fig. 2. Nitrogen physisorption isotherms for Fe/ZSM-5 and 2Fe/Al$_2$O$_3$.

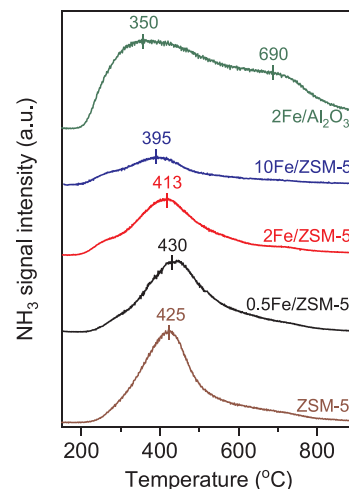**Fig. 3.** NH$_3$-TPD profiles of ZSM-5, Fe/ZSM-5, and 2Fe/Al$_2$O$_3$.

The surface acidity of Fe catalysts was investigated by NH$_3$-TPD experiments. The NH$_3$-TPD profiles for ZSM-5 and Fe/ZSM-5 samples showed a major desorption peak at around 420 °C (Fig. 3), which can be assigned to NH$_3$ strongly adsorbed on Brønsted acid sites in the form of ≡Si−OH−Al≡ [38–40]. With increasing Fe loading, there was a notable decrease in the peak intensity and desorption temperature, indicating that the surface acidity of Fe/ZSM-5 was reduced in both quantity and strength. In a previous study [41], by the adsorption of perfluorotributyl amine it has been determined that over 96% of the Brønsted acid sites of the HZSM-5 zeolite were located inside the zeolitic channels. Accordingly, it is reasonable to infer that part of the Fe species should have migrated into the zeolitic channels, where the Brønsted acid protons on the internal surface of the zeolite are replaced by the Fe ions. This is in accord with the N$_2$ physisorption results discussed above. On the other hand, 2Fe/Al$_2$O$_3$ showed two broad desorption peaks at around 350 and 690 °C, corresponding to medium and strong acid sites on the catalyst, respectively [42,43]. Notably, the total amount of acid sites on 2Fe/Al$_2$O$_3$ is about three times of that on 2Fe/ZSM-5 (Table 3).

3.3. Structure of Fe species in the Fe catalysts before and after reaction

The XRD patterns of as-prepared Fe/ZSM-5 catalysts showed the typical diffraction peaks of MFI-type structure (Fig. 4A), indicating that the crystalline nature of zeolites was maintained without any structural change upon the incorporation of Fe. No diffraction peaks characteristic of iron phases could be seen from the XRD patterns of 0.5Fe/ZSM-5, 2Fe/ZSM-5, and 2Fe/Al$_2$O$_3$, suggesting that Fe species should be highly dispersed in the catalysts. As the Fe loading increased to 10 wt%, additional diffraction peaks at 2θ = 33.2°, 35.7°, and 53.6° characteristic of α-Fe$_2$O$_3$ phase [30,44,45] emerged (see inset of Fig. 4A), pointing to the formation of large crystallites of Fe oxide at high Fe loading. After reaction, the XRD patterns of the spent Fe/ZSM-5 catalysts showed no appreciable changes compared with that before reaction (Fig. 4B), indicating that the structure of the Fe-modified ZSM-5 zeolite remained intact under reaction conditions. Similar result was obtained for the 2Fe/Al$_2$O$_3$ catalyst. Moreover, no characteristic diffractions from reduced iron oxides, metallic iron, or iron carbides could be identified from the XRD patterns of 0.5Fe/ZSM-5, 2Fe/ZSM-5, and 2Fe/Al$_2$O$_3$. In contrast, the XRD pattern of 10Fe/ZSM-5 showed additional weak diffraction peaks at 42.9° and 43.7° (see inset of Fig. 4B), which could be attributed to Fe$_3$C (cementite) phase [30,45]. Similar results have been reported previously for Fe/ZSM-5 catalysts subject to methane

aromatization reaction for several hours [30,45]. Analogously, in a recent study [29], the Fe$_3$C phase was also detected on the phosphorous-modified Fe/Al$_2$O$_3$ catalysts after reaction in propane dehydrogenation at 600 °C for 6 h. It has been suggested that Fe$_2$O$_3$ in the fresh catalyst would be reduced and carburized stepwise under non-oxidative reaction conditions of alkane activation, i.e., Fe$_2$O$_3$→α-Fe metal→Fe$_3$C [30,45].

The morphology and the crystallite size of Fe oxides on the Fe/ZSM-5 catalysts were examined by TEM (Fig. 5). Small aggregated Fe oxide clusters in size of a few nanometers can be resolved in the porous zeolite matrix on the as-prepared 0.5Fe/ZSM-5 and 2Fe/ZSM-5 (Fig. 5a and b). Apparently, these Fe oxide clusters are dispersed on the external surfaces of the zeolite support in view of its much smaller pore sizes (< 1 nm). Note that the presence of Fe species in the zeolitic channels, as deduced from the N$_2$ adsorption and NH$_3$-TPD results, could not be verified by these TEM images given its low resolution. Fe oxide nanoparticles became distinct on 10Fe/ZSM-5, with particle sizes of ˜20 nm (Fig. 5c), in good agreement with the XRD result. For 2Fe/Al$_2$O$_3$, Fig. 5d shows that the Al$_2$O$_3$ support has uniform and fine particle size of around 10 nm. It was, however, difficult to distinguish between the iron and alumina oxidic structures in the nanometer scale. The high-angle annular dark-field scanning transmission electron microscopy (HAADF-STEM) images (Fig. S3) indicate that the Fe oxide nanoparticles (brighter spots) are evenly distributed in these materials with particle sizes in the range of a few nanometers.

The morphology of 0.5Fe/ZSM-5 was hardly affected after reaction (Fig. 5e), whereas some large Fe particles (> 10 nm) could be clearly seen from the TEM images of the used 2Fe/ZSM-5 (Fig. 5f) and 10Fe/ZSM-5 (Fig. 5g). The sizes of Fe particles in both 2Fe/ZSM-5 and 10Fe/ZSM-5 exhibited a broad distribution in the range of a few nanometers to ca. 50 nm. Note that despite the marked degree of particle growth in the used 2Fe/ZSM-5, no reflections associated with Fe or Fe oxide crystallites were detected by XRD. This is likely due to the relatively low amount of Fe loading. In addition, high-resolution TEM images clearly showed that part of the Fe nanoparticles, especially those large ones (above 10 nm), were encapsulated in layers of carbon species (Fig. S4). Elemental analysis by EDX indicates that carbon deposits also existed on the surface of the zeolite support (Fig. S5). Compared with 2Fe/ZSM-5, the changes in the Fe morphology is less obvious for the used 2Fe/Al$_2$O$_3$ (Figs. 5 h and S3) and carbon deposition was also evidenced by EDX analysis (see Fig. S6).
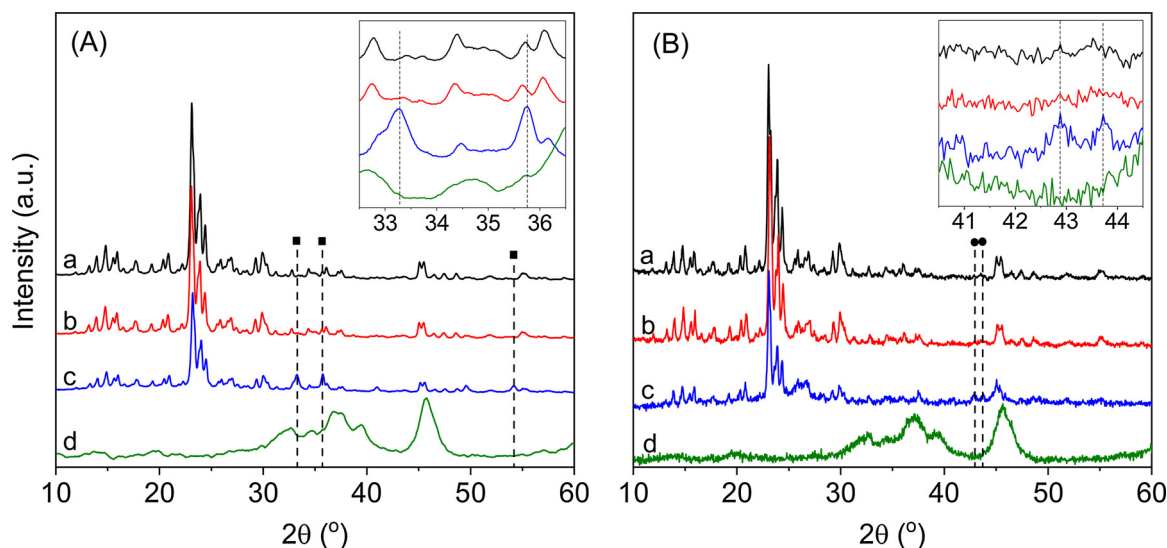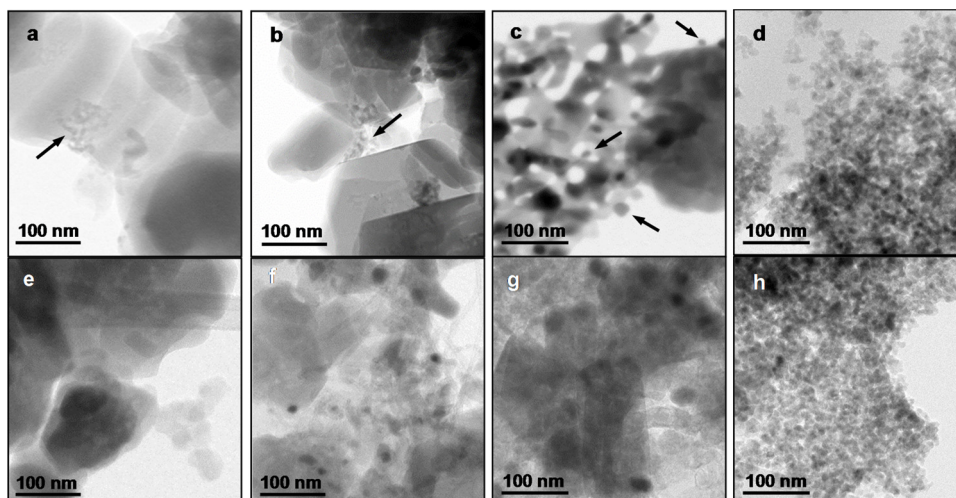

Fig. 4. XRD patterns of Fe/ZSM-5 and 2Fe/Al$_2$O$_3$ catalysts (A) before and (B) after reaction. (a) 0.5Fe/ZSM-5, (b) 2Fe/ZSM-5, (c) 10Fe/ZSM-5, (d) 2Fe/Al$_2$O$_3$. (squf;) α-Fe$_2$O$_3$, (cirf;) Fe$_3$C.

Fig. 5. Representative TEM images of fresh (upper panel) and spent (lower panel) Fe/ZSM-5 and 2Fe/Al$_2$O$_3$. (a,e) 0.5Fe/ZSM-5, (b,f) 2Fe/ZSM-5, (c,g) 10Fe/ZSM-5, and (d,h) 2Fe/Al$_2$O$_3$. Fe oxide clusters or nanoparticles are indicated by arrows.

3.4. Surface chemical states and compositions of Fe catalysts before and after reaction

The Fe 2p XPS spectra of the as-prepared Fe/ZSM-5 comprised two components at BE of ˜710.5 eV (Fe 2p$_{3/2}$) and ˜723.7 eV (Fe 2p$_{1/2}$), respectively, with a spin–orbit coupling energy gap of ca. 13.6 eV (Fig. 6A and Fig. S7). Both peaks are accompanied by distinct satellite peaks at around 718.4 and 732.6 eV. These features are characteristic of Fe oxides [30,46–48]. A deconvolution analysis of the spectra revealed the existence of both Fe^{3+} (711.7 eV) and Fe^{2+} (709.6 eV) species on the surface of all three Fe/ZSM-5 samples. The presence of Fe^{2+} may result from surface reduction under the ultrahigh vacuum conditions and X-ray flux of the measurement [48]. Similar results were derived for as-prepared 2Fe/Al$_2$O$_3$ (Fig. 6B).

To investigate the chemical states of Fe species under reaction conditions, the Fe/ZSM-5 catalysts were exposed to EDH reaction conditions at 600 °C for 30 min without any reduction pretreatment in a reaction cell that is attached to the XPS analysis chamber. The Fe/ZSM-5 samples were transferred immediately to the analysis chamber after reaction without exposure to air in between. Therefore, the information obtained thereby should reflect the surface chemical states of the catalysts under *in situ* conditions. The Fe 2p XPS signals were significantly attenuated after reaction for all samples (Figs. 6A and S7), especially for 2Fe/ZSM-5 and 10Fe/ZSM-5, mainly due to the coverage of Fe particles by large amount of carbon species, as shown by the TEM results above. The main characteristic features of oxidic Fe species could still be identified after reaction, indicative of incomplete reduction during the relatively short exposure time in the reaction atmosphere. Nevertheless, two new peaks with almost comparable signal intensities to that of oxidic Fe species emerged at BE of 707.1 eV and 705.5 eV, which could be ascribed to the formation of carbide species and metallic Fe [30,48–52], respectively. In contrast, no such species were detected on the used 2Fe/Al$_2$O$_3$, which only showed the characteristic peak of Fe^{2+} (Fig. 6B). Notably, the total fraction of these two new species steadily increases with the Fe loading, from 28% for 0.5Fe/ZSM-5 to 41% for 2Fe/ZSM-5 and 59% for 10Fe/ZSM-5, while the relative abundance of the carbide and metallic Fe species seemed to be less affected by the Fe loading (see Fig. S7 and Table 4).
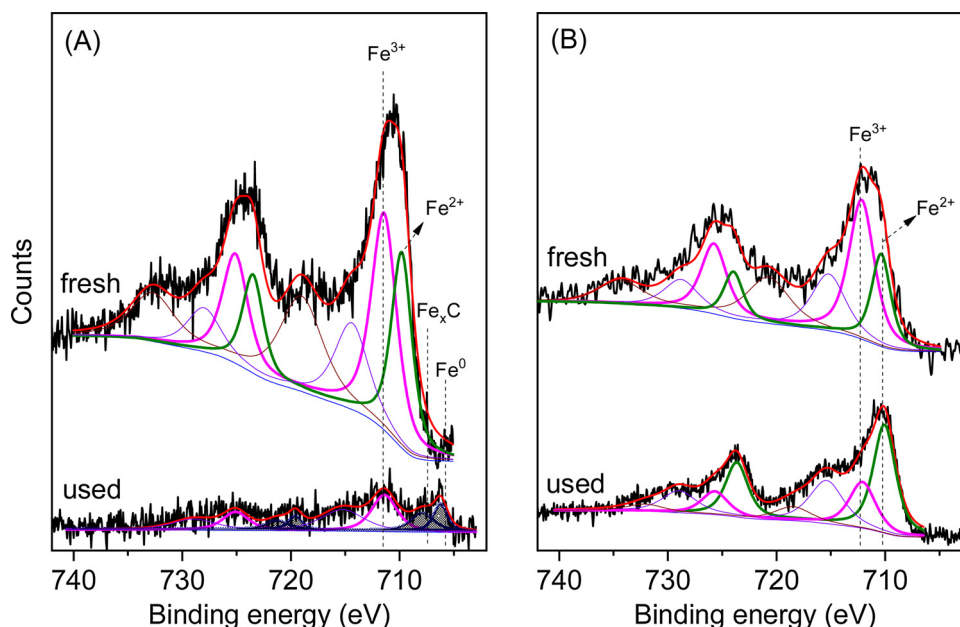
Fig. 6. Fe2p XPS spectra of (A) 2Fe/ZSM-5 and (B) 2Fe/Al$_2$O$_3$ before and after reaction for 30 min.

Table 4
Deconvolution analysis of Fe2p XPS spectra of Fe/ZSM-5 and 2Fe/Al$_2$O$_3$ after reaction for 30 min.

Catalyst	Fraction of Fe species (%)			
	Fe^{3+} or Fe^{2+}	Fe$_x$C	Fe^0	Fe$_x$C + Fe^0
0.5Fe/ZSM-5	61	20	19	39
2Fe/ZSM-5	54	24	22	46
10Fe/ZSM-5	42	17	41	58
2Fe/Al$_2$O$_3$	100	0	0	0

The formation of carburized Fe species on Fe/ZSM-5 during the EDH reaction was also evidenced by the C1s XPS spectra (Fig. 7A and S8). Graphitic carbon species at 284.6 eV dominates on the freshly calcined 2Fe/ZSM-5, accompanied by certain amount of carbon oxygenates (BE > 284.6 eV) [30,53]. After exposure to EDH reaction at 600 °C for 30 min, the BE of the main C1s signal shifted from 284.6 eV to ~283 eV (Fig. 7A), pointing to the formation of chemisorbed carbon during the EDH reaction [30,53–56]. The amount of the chemisorbed carbon species increases significantly by an order of magnitude with the Fe content in the Fe/ZSM-5 catalysts (Fig. S8), in accord with the coking analysis results (see below, Table 1). The deconvolution analysis further revealed an additional shoulder peak at ca. 283.7 eV on all the three Fe/ZSM-5 samples, which can be attributed to iron carbide species [30,53–56]. In contrast, only a small peak of chemisorbed carbon species at 282.5 eV was detected on the 2Fe/Al$_2$O$_3$ catalyst after reaction for 30 min (Fig. 7B).

The near-surface composition analysis results derived from the XPS data indicate that the surface atomic concentration of each element for 0.5Fe/ZSM-5 catalyst only slightly changed after reaction. In contrast, there was a significant decrease in the surface concentration of all elements except for carbon on 2Fe/ZSM-5 and 10Fe/ZSM-5. Note that the surface Si/Al ratio decreased most significantly from 20 on the as-prepared 10Fe/ZSM-5 to 10 after reaction (Table 5). This may be an indication that the Si sites are preferentially covered by carbon deposits or reaction-induced dealumination occurred for 10Fe/ZSM-5 leading to relative enrichment of Al on the surface.

The amount of deposited carbon on the spent Fe/ZSM-5 catalysts was quantitatively analyzed by TGA in an oxidizing atmosphere. Note that the catalysts were exposed to reaction atmosphere for extended reaction time (15 h) to increase the amount of carbon deposits intentionally to minimize the error in the quantification analysis. The amount of weight loss due to coke combustion was determined to be

Table 5
Surface atomic concentration of Fe/ZSM-5 catalysts determined by XPS before and after reaction for 30 min.

Catalyst		Atomic concentration (at.%)					
		Fe	C	Si	Al	O	Si/Al ratio
0.5Fe/ZSM-5	Fresh	0.6	6.7	26.8	1.5	63.4	18
	Used	0.4	10.0	25.4	1.6	62.6	16
2Fe/ZSM-5	Fresh	1.4	4.6	26.9	1.5	64.7	18
	Used	0.5	45.0	16.3	1.0	37.2	16
10Fe/ZSM-5	Fresh	6.3	5.6	24.5	1.2	61.6	20
	Used	0.5	88.4	3.1	0.3	7.7	10
2Fe/Al$_2$O$_3$	Fresh	2.3	7.0	–	36.9	53.7	–
	Used	1.2	14.3	–	31.9	52.1	–

0.005, 0.049, and 0.172 g·g$_{cat}$$^{-1}$ for 0.5Fe/ZSM-5, 2Fe/ZSM-5, and 10Fe/ZSM-5, respectively (see also Table 1). On the 2Fe/Al$_2$O$_3$ sample, a surprisingly higher amount of coke deposits was obtained, 0.268 g·g$_{cat}$$^{-1}$, after the same length of reaction time.

3.5. Nature of active sites on Fe/ZSM-5 for EDH reaction

Kinetic experiments resulted in comparable apparent E_a on the three Fe/ZSM-5 catalysts for EDH reaction, reflecting that different Fe loadings do not change the reaction mechanism. Most likely, the nature of active sites for EDH reaction remains the same as the Fe loading increases. Accordingly, the reaction rate per active site on different Fe/ZSM-5 catalysts is anticipated to be comparable under the same reaction conditions. In line with this postulation, the Fe-normalized reaction rate of ethane was almost identical on 0.5Fe/ZSM-5 and 2Fe/ZSM-5 (see Table 1), which also implies that the active Fe species are well dispersed when the Fe loading is below 2 wt%. The significantly lower reaction rate on 10Fe/ZSM-5 may be rationalized by the fact that the amount of active Fe species on 10Fe/ZSM-5 was overestimated due to the presence of large Fe oxide particles, since the calculation of reaction rates was based on the total amount of Fe instead of the surface Fe.

The Fe/ZSM-5 catalysts initially showed a rapid increase in ethane conversion to different extents before reaching a maximum after 30 min of reaction (see Fig. 1A). On 10Fe/ZSM-5, concomitant with the activity enhancement, there was also an improvement in the selectivity of ethylene, with a dramatic increase from 18% to ~70% (see Fig. 1B). This behavior may be induced by the structure transformation in the as-prepared Fe/ZSM-5 catalysts upon exposure to reaction conditions, leading to the generation of intrinsically more active and selective sites
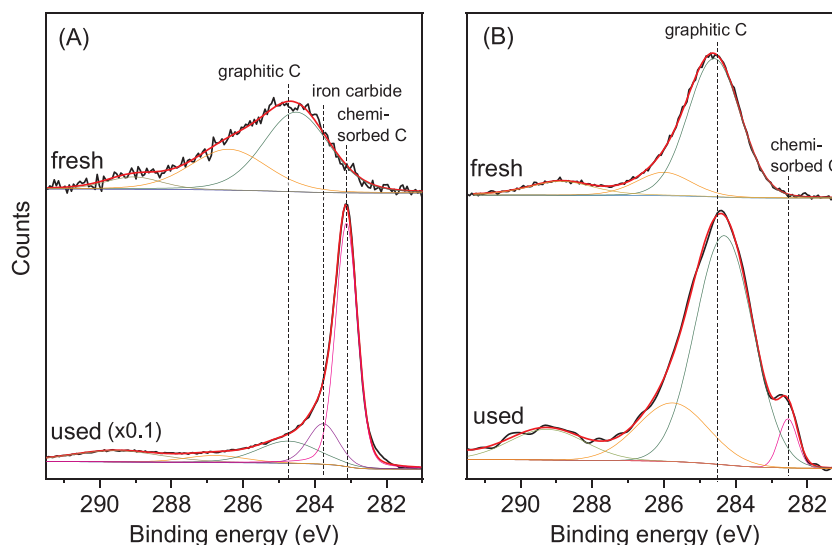

Fig. 7. C1s XPS spectra of (A) 2Fe/ZSM-5 and (B) 2Fe/Al$_2$O$_3$ before and after reaction for 30 min.

for EDH reaction. This presumption is corroborated by the *in situ* XPS results, which clearly showed that during the activation period of 30 min the iron oxides underwent partial reduction and carburization. Quantitative analysis revealed that the total fraction of the reduced and carburized Fe species scaled with the Fe loading (Table 4). Therefore, it is very likely that both metallic Fe and Fe carbides are catalytically active species for the ethane activation. Moreover, the XRD pattern of 10Fe/ZSM-5 after reaction for 270 min clearly indicated that at this stage carburized Fe species dominated in the bulk phase although the existence of metallic Fe could not be excluded considering the detection limit of XRD technique. Accordingly, we speculate that the extent of Fe carburization may increase with extended reaction time. Similar evolution of Fe species from Fe metal to Fe carbide with reaction time for a few hours has been reported recently for Fe/ZSM-5 catalysts in non-oxidative aromatization of methane [30] and for phosphorous-modified Fe/Al_2O_3 catalysts in propane dehydrogenation [29]. In both cases, it was found that only after the iron carbide phase appears do the re-activity and selectivity achieve steady-state conditions with good activity and high selectivity of aromatic products or propylene [29,30]. Accordingly, the Fe carbide species have been proposed to be the real active sites for either methane or propane activation [29,30].

Note that the dramatic increase in ethylene selectivity was not observed on either 0.5Fe/ZSM-5 or 2Fe/ZSM-5. The discrepancy is probably related to the significantly lower Fe loadings and smaller crystallite sizes of Fe oxides, which could affect the kinetics and thus the extent of reduction and carburization of the Fe oxide species [57,58]. Based on the XPS results in Tables 4 and 5, the extent of Fe oxide reduction and carbon deposition on 10Fe/ZSM-5 is significantly greater than that for the other two catalysts. The initially large fraction and total amount of metallic Fe species on the surface of 10Fe/ZSM-5 may account for its very low initial selectivity, while this effect is not that obvious on the other two catalysts with low Fe loadings.

In order to further understand the dehydrogenation mechanism of ethane and discriminate the different possible active sites on Fe/ZSM-5 catalysts, DFT calculations were performed on three model catalysts, representing iron oxide, metallic iron, and iron carbide supported on ZSM-5 zeolite (Figs. S9 and S10). The results showed that the energy profile of ethane conversion to adsorbed ethyl intermediates is comparable on either metallic or carburized Fe, indicating that both Fe species are active for ethane activation, in line with the experimental results discussed above. The desorption of the ethylene product from the surface is found to be the most energy demanding step, requiring about 2.0 and 1.2 eV on metallic Fe and carburized Fe surface, respectively (see Fig. 8). Interestingly, the experimentally determined apparent E_a of ethane conversion to ethylene on these catalysts is about 110 kJ·mol^{-1}, equal to 1.14 eV (Table 1), which agrees very well with the theoretical desorption energy on carburized Fe. This coincidence

strongly suggests that iron carbide species should be the major active sites for EDH reaction under steady state conditions. This deduction is supported by the XRD results that no Fe metal but only Fe_3C phase was detected by XRD after reaction for 270 min (Fig. 4B). In addition, the DFT calculations demonstrate that compared with the direct C_2H_4 desorption from Fe metal, the carburization of Fe metal associated with C_2H_4 decomposition is energetically more favorable (see dash line in Fig. 8). Therefore, the metallic Fe species, after being formed initially, will be carburized gradually with time. These results further indicate that carburized Fe species is intrinsically more energetically stable and catalytically selective to ethylene product under the EDH reaction conditions. Note that the decrease in conversion after 30 min of reaction does not necessarily point to the lower activity of the carbide species than that of the Fe metal sites. Rather, this may result from the growth in Fe particle size with time and continuous deposition of carbon species, which decreased the total number of available active sites on the catalyst surface. Furthermore, there seems to be no direct correlation between the abundance of metallic and/or carburized Fe species with the specific reaction rates, namely, 2Fe/ZSM-5 has a comparable reaction rate to that of 0.5Fe/ZSM-5 despite its higher fraction of Fe$_x$C + Fe^0 species on the surface (see Tables 1 and 4). This may be due to the different extents of agglomeration of the Fe nano-particles in these two catalysts. It is also likely that the Fe carbide species consist of various phases with different intrinsic activities [59,60], which could not be distinguished by XPS.

The DFT calculations also show that reaction of ethane over iron oxide, forming H_2O, C_2H_4, and reduced iron species (as in -Fe$_2$O-), is the most energetically favored pathway (Fig. 8). Accordingly, considering the reductive and non-oxidative environment under reaction conditions, Fe^{3+} would most likely be reduced and transformed to lower oxidation states or carbides shortly in the absence of external oxygen sources.

3.6. Effect of support on the catalytic performances of Fe catalysts in EDH reaction

The results presented in Fig. 1 and Table 1 clearly showed that there is a remarkable effect of support material on the catalytic behaviors of Fe catalysts in the EDH reaction. The 2Fe/ZSM-5 catalysts are far superior to that of Al_2O_3-supported counterpart in terms of both ethane conversion and ethylene selectivity. Note that the different calcination conditions should not be responsible for the remarkable support effect. This is corroborated by the fact that Fe/Al_2O_3 calcined by the two different procedures showed almost identical NH_3-TPD profiles and comparable activities in the EDH reaction (see Fig. S11). Based on the discussion in the previous section, the discrepancy in the activity of these two types of catalysts may be attributed to the ease in the
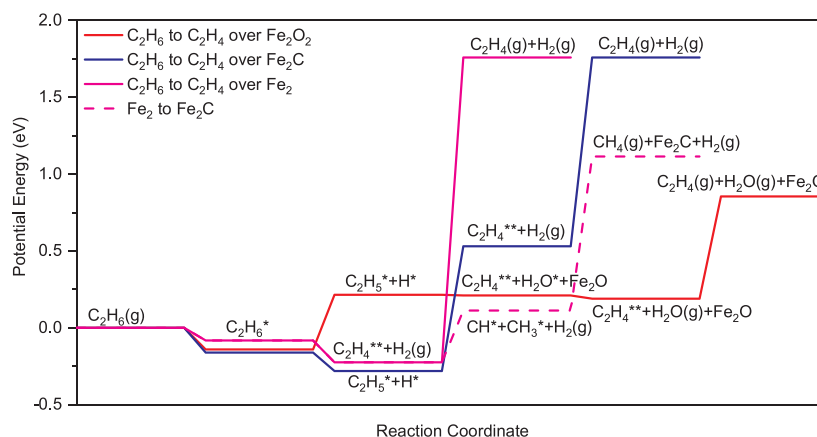

Fig. 8. Potential energy profiles of C_2H_6 conversion to C_2H_4 over iron oxide, metallic iron, and iron carbide. The dashed pink line represents cracking of C_2H_6 over metallic iron forming CH_4 and Fe_2C.
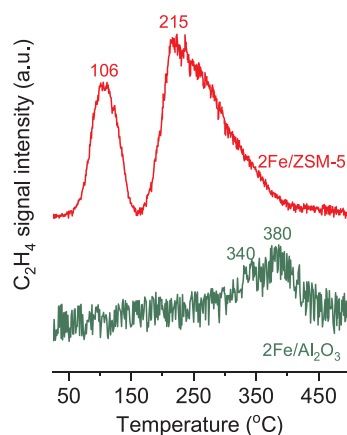
Fig. 9. C_2H_4-TPD profiles of 2Fe/ZSM-5 and 2Fe/Al$_2$O$_3$.

formation of active metallic and/or iron carbide species, as evidenced by the XPS results, which showed that no such species are formed on the 2Fe/Al$_2$O$_3$ catalyst under the same conditions (Figs. 6B and 7 B). We surmise that Fe could form mixed oxides with the Al$_2$O$_3$ support, namely, surface iron aluminates, which are difficult to reduce and could hinder the formation of the active iron carbide phase [61]. The different chemical states of Fe species under reaction conditions may result in a different reaction mechanism, which is reflected by the notably higher (by 30 kJ·mol^{-1}) apparent E_a determined on 2Fe/Al$_2$O$_3$ compared with that on Fe/ZSM-5. We note that the apparent E_a determined on Fe/Al$_2$O$_3$ should be valid for comparing with that of Fe/ZSM-5 despite its lower selectivity to ethylene, which primarily resulted from the different extents of consecutive reactions of ethylene intermediate rather than a different parallel reaction pathway such as C-C cleavage during ethane activation. This is supported by the extremely low selectivity (0.1%) of the methane product on 2Fe/Al$_2$O$_3$, which is even lower than that on Fe/ZSM-5 (1.3%).

On the other hand, the significantly lower selectivity on the 2Fe/Al$_2$O$_3$ catalyst may originate from its different adsorption/desorption behavior of the ethylene product on the surface. It is generally accepted that byproducts of EDH reaction, such as methane, higher hydrocarbons, and carbon deposits, are formed by consecutive reaction of the adsorbed ethylene product [3,9]. To verify this point, we have performed C_2H_4-TPD experiment on the 2Fe/Al$_2$O$_3$ and 2Fe/ZSM-5 catalysts. The results in Fig. 9 clearly showed that ethylene tends to desorb from the surface of Fe/Al$_2$O$_3$ at much higher temperatures, by over 100 °C, than that from Fe/ZSM-5. Apparently, the strong binding of the ethylene product on the Fe/Al$_2$O$_3$ catalyst would significantly increase its residence time on the surface thus facilitating its further transformation into higher hydrocarbon products or carbonaceous materials, particularly in the presence of strong acid sites. This is further substantiated by the findings that the total amount of acid sites on 2Fe/Al$_2$O$_3$ is about 3 times of that on 2Fe/ZSM-5 (see Table 3) and that with extended reaction time, significantly higher amount of carbon deposits, by a factor of 5, was detected on 2Fe/Al$_2$O$_3$ (see Table 1). Note that longer residence time of ethylene product on the catalyst, especially acid sites on the support, could lead to extensive carbon formation but not necessarily the subsequent Fe carburization since these two processes are expected to occur at different locations on the catalyst.

4. Conclusion

We have demonstrated that iron supported on ZSM-5 zeolite is an efficient catalyst system for the non-oxidative dehydrogenation reaction of ethane to ethylene. The iron-based catalysts exhibited the best stability and the highest steady-state activity towards ethylene production under the same reaction conditions, compared with Pt/ZSM-5, PtSn/Al$_2$O$_3$, and various metal oxide catalysts. The zeolite support

proves to be the key to achieve optimal activity of iron catalysts, in view of its much higher ethane conversion than that on conventional γ-Al$_2$O$_3$ support. The activity of the Fe/ZSM-5 catalysts can be effectively enhanced by increasing the iron loading. In addition, the production rate of ethylene on the Fe/ZSM-5 catalyst can be further enhanced by lowering the total flow rate as well as by increasing the concentration of ethane in the feed gas. The characterization results indicated that increasing the Fe loading beyond 2 wt% led to the formation of large Fe crystallites. Based on the XRD, *in situ* XPS, and DFT calculation results, both metallic and carburized iron are suggested to be catalytically active for the EDH reaction, with the latter being more stable and selective toward ethylene formation. The superior performance of Fe/ZSM-5 catalysts to that of Fe/Al$_2$O$_3$ is attributed to the facile formation of metallic and/or carburized iron species. The relatively weaker binding strength of ethylene product and the weaker surface acidity on Fe/ZSM-5 allows rapid desorption of ethylene once formed and suppresses its consecutive transformation into higher hydrocarbon products and carbon deposits.

Appendix A. Supplementary data

Supplementary material related to this article can be found, in the online version, at doi:https://doi.org/10.1016/j.apcatb.2019.117816.

References

[1] M. Bhasin, J. McCain, B. Vora, T. Imai, P. Pujado, Dehydrogenation and oxydehydrogenation of paraffins to olefins, Appl. Catal. A Gen. 221 (2001) 397–419.

[2] D. Sanfilippo, I. Miracca, Dehydrogenation of paraffins: synergies between catalyst design and reactor engineering, Catal. Today 111 (2006) 133–139.

[3] J.J. Sattler, J. Ruiz-Martinez, E. Santillan-Jimenez, B.M. Weckhuysen, Catalytic dehydrogenation of light alkanes on metals and metal oxides, Chem. Rev. 114 (2014) 10613–10653.

[4] F. Cavani, N. Ballarini, A. Cericola, Oxidative dehydrogenation of ethane and propane: how far from commercial implementation, Catal. Today 127 (2007) 113–131.

[5] H. Chen, L. Li, J. Hu, Upgrading of stranded gas via non-oxidative conversion processes, Catal. Today 310 (2018) 94–97.

[6] E. Gobina, R. Hughes, Ethane dehydrogenation using a high-temperature catalytic membrane reactor, J. Membr. Sci. 90 (1994) 11–19.

[7] A.M. Champagnie, T.T. Tsotsis, R.G. Minet, E. Wagner, The study of ethane dehydrogenation in a catalytic membrane reactor, J. Catal. 134 (1992) 713–730.

[8] D. Ding, Y. Zhang, W. Wu, D. Chen, M. Liu, T. He, A novel low-thermal-budget approach for the co-production of ethylene and hydrogen via the electrochemical non-oxidative deprotonation of ethane, Energy Environ. Sci. 11 (2018) 1710–1716.

[9] V. Galvita, G. Siddiqi, P. Sun, A.T. Bell, Ethane dehydrogenation on Pt/Mg(Al)O and PtSn/Mg(Al)O catalysts, J. Catal. 271 (2010) 209–219.

[10] G. Siddiqi, P. Sun, V. Galvita, A.T. Bell, Catalyst performance of novel Pt/Mg(Ga) (Al)O catalysts for alkane dehydrogenation, J. Catal. 274 (2010) 200–206.

[11] P. Sun, G. Siddiqi, M. Chi, A.T. Bell, Synthesis and characterization of a new catalyst Pt/Mg(Ga)(Al)O for alkane dehydrogenation, J. Catal. 274 (2010) 192–199.

[12] P. Sun, G. Siddiqi, W.C. Vining, M. Chi, A.T. Bell, Novel Pt/Mg(In)(Al)O catalysts for ethane and propane dehydrogenation, J. Catal. 282 (2011) 165–174.

[13] H. Xiong, S. Lin, J. Goetze, P. Pletcher, H. Guo, L. Kovarik, K. Artyushkova, B.M. Weckhuysen, A.K. Datye, Thermally stable and regenerable platinum–Tin clusters for propane dehydrogenation prepared by atom trapping on Ceria, Angew. Chem. Int. Ed. 56 (2017) 8986–8991.

[14] C.-T. Shao, W.-Z. Lang, X. Yan, Y.-J. Guo, Catalytic performance of gallium oxide based-catalysts for the propane dehydrogenation reaction: effects of support and loading amount, RSC Adv. 7 (2017) 4710–4723.

[15] P.L. De Cola, R. Gläser, J. Weitkamp, Non-oxidative propane dehydrogenation over Pt–Zn-containing zeolites, Appl. Catal. A Gen. 306 (2006) 85–97.

[16] M.W. Schreiber, C.P. Plaisance, M. Baumgärtl, K. Reuter, A. Jentys, R. Bermejo-Deval, J.A. Lercher, Lewis–Brønsted acid pairs in Ga/H-ZSM-5 to catalyze dehydrogenation of light alkanes, J. Am. Chem. Soc. 140 (2018) 4849–4859.

[17] S. Sokolov, M. Stoyanova, U. Rodemerck, D. Linke, E.V. Kondratenko, Comparative study of propane dehydrogenation over V-, Cr-, and Pt-based catalysts: time on-stream behavior and origins of deactivation, J. Catal. 293 (2012) 67–75.

[18] Z.J. Zhao, T. Wu, C. Xiong, G. Sun, R. Mu, L. Zeng, J. Gong, Hydroxyl-Mediated Non-oxidative Propane Dehydrogenation over VO$_x$/γ-Al$_2$O$_3$ Catalysts with Improved Stability, Angew. Chem. Int. Ed. 57 (2018) 6791–6795.

[19] P. Mitchell, S. Wass, Propane dehydrogenation over molybdenum hydrotalcite catalysts, Appl. Catal. A Gen. 225 (2002) 153–165.

[20] N.M. Schweitzer, B. Hu, U. Das, H. Kim, J. Greeley, L.A. Curtiss, P.C. Stair, J.T. Miller, A.S. Hock, Propylene hydrogenation and propane dehydrogenation by a single-site Zn^{2+} on silica catalyst, ACS Catal. 4 (2014) 1091–1098.

[21] J. Camacho-Bunquin, P. Aich, M. Ferrandon, U. Das, F. Dogan, L.A. Curtiss, J.T. Miller, C.L. Marshall, A.S. Hock, P.C. Stair, Single-site zinc on silica catalysts for propylene hydrogenation and propane dehydrogenation: synthesis and reactivity evaluation using an integrated atomic layer deposition-catalysis instrument, J. Catal. 345 (2017) 170–182.

[22] V.J. Cybulskis, B.C. Bukowski, H.-T. Tseng, J.R. Gallagher, Z. Wu, E. Wegener, A.J. Kropf, B. Ravel, F.H. Ribeiro, J. Greeley, Zinc promotion of platinum for catalytic light alkane dehydrogenation: insights into geometric and electronic effects, ACS Catal. 7 (2017) 4173–4181.

[23] A. Virnovskaia, E. Rytter, U. Olsbye, Kinetic and isotopic study of ethane dehydrogenation over a semicommercial Pt,Sn/Mg(Al)O catalyst, Ind. Eng. Chem. Res. 47 (2008) 7167–7177.

[24] E.H. Lee, Iron oxide catalysts for dehydrogenation of ethylbenzene in the presence of steam, Catal. Rev. 8 (1974) 285–305.

[25] M. Mediero-Munoyerro, J. McGregor, L. McMillan, N. Al-Yassir, P. Bingham, S. Forder, C. Gorin, S. Al-Khattaf, L. Gladden, P. Midgley, Structural changes in FeO$_x$/γ-Al$_2$O$_3$ catalysts during ethylbenzene dehydrogenation, Catal. Struct. React. 2 (2016) 25–32.

[26] B. Hu, N.M. Schweitzer, G. Zhang, S.J. Kraft, D.J. Childers, M.P. Lanci, J.T. Miller, A.S. Hock, Isolated Fe^{II} on silica as a selective propane dehydrogenation catalyst, ACS Catal. 5 (2015) 3494–3503.

[27] H.M.T. Galvis, J.H. Bitter, C.B. Khare, M. Ruitenbeek, A.I. Dugulan, K.P. de Jong, Supported iron nanoparticles as catalysts for sustainable production of lower olefins, Science 335 (2012) 835–838.

[28] Y. Sun, Y. Wu, H. Shan, G. Wang, C. Li, Studies on the promoting effect of sulfate species in catalytic dehydrogenation of propane over Fe$_2$O$_3$/Al$_2$O$_3$ catalysts, Catal. Sci. Technol. 5 (2015) 1290–1298.

[29] S. Tan, B. Hu, W.-G. Kim, S.H. Pang, J.S. Moore, Y. Liu, R.S. Dixit, J.G. Pendergast, D.S. Sholl, S. Nair, Propane dehydrogenation over alumina-supported Iron/Phosphorus catalysts: structural evolution of Iron species leading to high activity and propylene selectivity, ACS Catal. 6 (2016) 5673–5683.

[30] P. Tan, Active phase, catalytic activity, and induction period of Fe/zeolite material in nonoxidative aromatization of methane, J. Catal. 338 (2016) 21–29.

[31] J.H. Yun, R.F. Lobo, Catalytic dehydrogenation of propane over iron-silicate zeolites, J. Catal. 312 (2014) 263–270.

[32] G. Kresse, J. Furthmüller, Efficient iterative schemes for ab initio total-energy calculations using a plane-wave basis set, Phys. Rev. B 54 (1996) 11169.

[33] J.P. Perdew, K. Burke, M. Ernzerhof, Generalized gradient approximation made simple, Phys. Rev. Lett. 77 (1996) 3865.

[34] P.E. Blöchl, Projector augmented-wave method, Phys. Rev. B 50 (1994) 17953.

[35] R. Barthos, A. Széchenyi, F. Solymosi, Decomposition and aromatization of ethanol on ZSM-based catalysts, J. Phys. Chem. B 110 (2006) 21816–21825.

[36] M. Iwamoto, Y. Kosugi, Highly selective conversion of ethene to propene and butenes on nickel ion-loaded mesoporous silica catalysts, J. Phys. Chem. C 111 (2007) 13–15.

[37] M. Shahami, K.M. Dooley, D.F. Shantz, Steam-assisted crystallized Fe-ZSM-5 materials and their unprecedented activity in benzene hydroxylation to phenol using hydrogen peroxide, J. Catal. 368 (2018) 354–364.

[38] C.V. Hidalgo, H. Itoh, T. Hattori, M. Niwa, Y. Murakami, Measurement of the acidity of various zeolites by temperature-programmed desorption of ammonia, J. Catal. 85 (1984) 362–369.

[39] D. Ma, W. Zhang, Y. Shu, X. Liu, Y. Xu, X. Bao, MAS NMR, ESR and TPD studies of Mo/HZSM-5 catalysts: evidence for the migration of molybdenum species into the zeolitic channels, Catal. Lett. 66 (2000) 155–160.

[40] J. Post, J. Van Hooff, Acidity and activity of H-ZSM-5 measured with NH$_3$-TPD and n-hexane cracking, Zeolites 4 (1984) 9–14.

[41] W. Zhang, D. Ma, X. Han, X. Liu, X. Bao, X. Guo, X. Wang, Methane dehydro-aromatization over Mo/HZSM-5 in the absence of oxygen: a multinuclear solid-state NMR study of the interaction between supported Mo species and HZSM-5 zeolite with different crystal sizes, J. Catal. 188 (1999) 393–402.

[42] V.S. Marakatti, D. Mumbaraddi, G.V. Shanbhag, A.B. Halgeri, S.P. Maradur, Molybdenum oxide/γ-alumina: an efficient solid acid catalyst for the synthesis of nopol by Prins reaction, RSC Adv. 5 (2015) 93452–93462.

[43] H. Xiao, J. Zhang, P. Wang, X. Wang, F. Pang, Z. Zhang, Y. Tan, Dehydrogenation of propane over a hydrothermal-synthesized Ga$_2$O$_3$–Al$_2$O$_3$ catalyst in the presence of carbon dioxide, Catal. Sci. Technol. 6 (2016) 5183–5195.

[44] A. Sacco Jr., P. Thacker, T.N. Chang, A.T. Chiang, The initiation and growth of filamentous carbon from α-iron in H$_2$, CH$_4$, H$_2$O, CO$_2$, and CO gas mixtures, J. Catal. 85 (1984) 224–236.

[45] S. Takenaka, M. Serizawa, K. Otsuka, Formation of filamentous carbons over supported Fe catalysts through methane decomposition, J. Catal. 222 (2004) 520–531.

[46] G. Bhargava, I. Gouzman, C. Chun, T. Ramanarayanan, S. Bernasek, Characterization of the "native" surface thin film on pure polycrystalline iron: a high resolution XPS and TEM study, Appl. Surf. Sci. 253 (2007) 4322–4329.

[47] M.C. Biesinger, B.P. Payne, A.P. Grosvenor, L.W. Lau, A.R. Gerson, R.S.C. Smart, Resolving surface chemical states in XPS analysis of first row transition metals, oxides and hydroxides: Cr, Mn, Fe, Co and Ni, Appl. Surf. Sci. 257 (2011) 2717–2730.

[48] D. Wilson, M. Langell, XPS analysis of oleylamine/oleic acid capped Fe$_3$O$_4$ nanoparticles as a function of temperature, Appl. Surf. Sci. 303 (2014) 6–13.

[49] C. Kuivila, J. Butt, P. Stair, Characterization of surface species on iron synthesis catalysts by X-ray photoelectron spectroscopy, Appl. Surf. Sci. 32 (1988) 99–121.

[50] J. Guo, R. Wang, W.W. Tjiu, J. Pan, T. Liu, Synthesis of Fe nanoparticles@graphene composites for environmental applications, J. Hazard. Mater. 225 (2012) 63–73.

[51] L. Yang, L. Pastor-Pérez, S. Gu, A. Sepúlveda-Escribano, T. Reina, Highly efficient Ni/CeO$_2$-Al$_2$O$_3$ catalysts for CO$_2$ upgrading via reverse water-gas shift: effect of selected transition metal promoters, Appl. Catal. B Environ. 232 (2018) 464–471.

[52] S. Kuppuswamy, J.D. Wofford, C. Joseph, Z.-L. Xie, A.K. Ali, V.M. Lynch, P.A. Lindahl, M.J. Rose, Structures, interconversions, and spectroscopy of iron carbonyl clusters with an interstitial carbide: localized metal center reduction by overall cluster oxidation, Inorg. Chem. 56 (2017) 5998–6012.

[53] G. Panzner, W. Diekmann, The bonding state of carbon segregated to α-iron surfaces and on iron carbide surfaces studied by electron spectroscopy, Surf. Sci. 160 (1985) 253–270.

[54] S. Hofmann, R. Sharma, C. Ducati, G. Du, C. Mattevi, C. Cepek, M. Cantoro, S. Pisana, A. Parvez, F. Cervantes-Sodi, In situ observations of catalyst dynamics during surface-bound carbon nanotube nucleation, Nano Lett. 7 (2007) 602–608.

[55] A. Wiltner, C. Linsmeier, Formation of endothermic carbides on iron and nickel, Phys. Stat. Sol. (a) 201 (2004) 881–887.

[56] B.M. Weckhuysen, M.P. Rosynek, J.H. Lunsford, Characterization of surface carbon formed during the conversion of methane to benzene over Mo/H-ZSM-5 catalysts, Catal. Lett. 52 (1998) 31–36.

[57] H.M.T. Galvis, J.H. Bitter, T. Davidian, M. Ruitenbeek, A.I. Dugulan, K.P. de Jong, Iron particle size effects for direct production of lower olefins from synthesis gas, J. Am. Chem. Soc. 134 (2012) 16207–16215.

[58] J. Xie, H.M.T. Galvis, A.C.J. Koeken, A. Kirilin, A.I. Dugulan, M. Ruitenbeek, K.P. de Jong, Size and promoter effects on stability of carbon-nanofiber-supported iron-based Fischer–Tropsch catalysts, ACS Catal. 6 (2016) 4017–4024.

[59] K. Xu, B. Sun, J. Lin, W. Wen, Y. Pei, S. Yan, M. Qiao, X. Zhang, B. Zong, ε-Iron carbide as a low-temperature Fischer–Tropsch synthesis catalyst, Nat. Comm. 5 (2014) 5783.

[60] C. Yang, H. Zhao, Y. Hou, D. Ma, Fe$_5$C$_2$ nanoparticles: a facile bromide-induced synthesis and as an active phase for Fischer–Tropsch synthesis, J. Am. Chem. Soc. 134 (2012) 15814–15821.

[61] A.F.H. Wielers, A.J.H.M. Kock, C.E.C.A. Hop, J.W. Geus, A.M. Van Der Kraan, The reduction behavior of silica-supported and alumina-supported iron catalysts: a Mössbauer and infrared spectroscopic study, J. Catal. 117 (1989) 1.